electronics

MDPI

Article

An Zero-Point Drift Suppression Method for eLoran Signal Based on a Segmented Inaction Algorithm

Miao Wu [1], Xianzhou Jin [1], Xin Qi [2], Jianchen Di [1], Tingyi Yu [1] and Fangneng Li [1,*]

[1] Naval University of Engineering, Wuhan 430033, China;
wumiao2652@163.com (M.W.); jxz2065629079@163.com (X.J.); 18202530626@163.com (X.Q.);
21100602@nue.edu.cn (J.D.); 19577772979@163.com (T.Y.)
[2] Chinese Peoples Liberat Army Troop 92678, Tianjin 300220, China
* Correspondence: fangneng_li@126.com

Abstract

Research on interference suppression technology for enhanced long-range navigation (eLoran) signals is crucial for enhancing receiver performance. To address the zero-point drift phenomenon in eLoran signals during adaptive filtering, we propose a segmented inaction algorithm based on normal time-frequency transform (NTFT), which is designed for challenging environments, such as low signal-to-noise ratio (SNR) and complex noise conditions. The algorithm splits the 20kHz frequency band of the eLoran signal into 200 equal sub-bands, then applies inaction algorithm sequentially to each sub-band, which exhibits strong noise resistance and high robustness. It is regarded as a pre-filter of the adaptive filter, ensuring a cleaner input signal for subsequent processing. Simulation results indicate that, when processing low SNR eLoran signals affected by multi-frequency narrow band interference and band-limited Gaussian noise, the combined algorithm significantly improves root mean square error (RMSE) by 33.3%, relative root mean square error (R-RMSE) by 39.1% compared to the single VSS-LMS method. Additionally, it compensates for zero-point drift by 79.3% and maintains third-week forward over-zero error at a very low level. The effectiveness of the combined algorithm was further validated through actual measurement experiments.

how to define zero-point drift percentage?

Keywords: zero-point drift; eLoran; narrow band interference; normal time-frequency transform; adaptive algorithm; variable step size least mean square algorithm

Academic Editor: Firstname Lastname

Received: date
Revised: date
Accepted: date
Published: date

Citation: To be added by editorial staff during production.

Copyright: © 2025 by the authors. Submitted for possible open access publication under the terms and conditions of the Creative Commons Attribution (CC BY) license (https://creativecommons.org/licenses/by/4.0/).

1. Introduction

Positioning, Navigation, and Timing (PNT) systems are essential for modern social and military operations. Satellite-based systems like global positioning system (GPS), global navigation satellite system (GLONASS), and BeiDou navigation satellite (BDS) dominate navigation and timing services due to their rapid development, high performance, and extensive coverage. However, these systems can be compromised by electromagnetic interference and environmental shielding, reducing their effectiveness. Thus, relying solely on satellite-based systems is not advisable. In response, many countries are developing eLoran as a reliable backup to the global navigation satellite system (GNSS) [1,2].

The eLoran system operates at a signal frequency of 100 kHz, with antenna transmission power reaching megawatt levels. It offers coverage up to 800 km on land and 150 km

at sea, providing time services with accuracy better than 100 ns and positioning services with a 20 m differential correction [3,4]. Thanks to its low-frequency propagation and high transmission power, eLoran can receive signals from land navigation stations even underwater, allowing real-time correction of time and position information. This capability makes it a crucial component of future underwater PNT systems [5,6].

The Loran system has evolved into the eLoran system, achieving positioning accuracy of up to 20 meters and stability of 95% [7]. Recent advancements in modern signal processing have led to the development of various eLoran interference suppression algorithms. These include methods based on the inverse fast Fourier transform (IFFT) spectral division [8], finite impulse response (FIR) band-pass filters for out-of-band interference [9], and all-phase fast Fourier transform (APFFT) notch filters for in-band point-frequency interference [10]. Additionally, the IFFT-derived multiple signal classification (MUSIC) algorithm addresses skywave interference [11], while comb filters suppress cross interference in static or low-speed conditions [12]. Wavelet techniques with specified soft thresholds and FIR filtering effectively reduce noise while preserving signal energy [13]. Most eLoran receivers utilize conventional FIR and IIR filters for signal processing [14]. The Dmeyer wavelet also selected for reconstructing weak eLoran signals [15].

Despite recent advancements, research has primarily concentrated on suppressing noise interference, while the zero-point drift phenomenon during signal processing remains largely unaddressed. This oversight results in deviations in the positioning accuracy of the eLoran receiver. Furthermore, these filtering algorithms are susceptible to strong interference, which can distort signals and compromise the reliability of receiver period identification. Consequently, their applicability is limited under harsh conditions.

The time difference measurement of the eLoran signal utilizes a zero-point phase tracking mode. In this approach, the measurement pulse follows the zero-crossing point of the eLoran signal during the third period via a phase-locked loop, enabling accurate time difference measurement. However, any drift in the zero point can result in a deviation of the measurement pulse's reference. Typically, the identification of the zero point in the third period relies on the waveform characteristics of the eLoran signal for accurate discrimination. Distortion of the waveform can introduce errors in period discrimination, leading to misalignment in phase tracking. Each instance of misalignment corresponds to a positional deviation of 3 kilometers.

The paper addresses the outlined problems by comparing existing methods and utilizing the normal time-frequency transform developed by Liu Lintao's research team at the Chinese Academy of Sciences [16,17]. This method, known as the NTFT, is applied to analyze eLoran signals in the time-frequency domain. We propose a segmented inaction method based on NTFT theory, which is integrated with a VSS-LMS adaptive filtering algorithm. In environments characterized by strong noise and low SNR, this approach effectively suppresses zero-point drift and waveform distortion, issues typically caused by single adaptive filters.

Consequently, it enhances eLoran signal reconstruction and zero-point drift suppression, ensuring reliability for subsequent demodulation and decoding processes.

The paper proposes a segmented inaction method utilizing NTFT to address the zero-point drift issue at the positive zero-crossing point in the third cycle of eLoran, which is caused by the adaptive filter VSS-LMS. **Section 2** introduces adaptive filtering and common filter algorithms, detailing the filtering principle of the piecewise non-action algorithm. It also selects an appropriate window function length for this algorithm based on simulation results. **Section** 3 simulates the correction of zero-point drift resulting from adaptive filtering, applying the proposed algorithm and comparing it to traditional filter algorithms. **Section** 4 evaluates the filtering algorithms using experimental data to

confirm the effectiveness of the proposed method. Finally, **Section 5** summarizes the findings of the paper.

what is antenna bottom current?

2. Adaptive Filtering Zero-Point Drift Suppression Algorithm

2.1 Mathematical Model of eLoran Signal

The eLoran signal is a phase-modulated pulse with a carrier frequency of 100 kHz and a pulse width of approximately 260 μs. The total out-of-band energy of the eLoran pulse constitutes less than 1% of the total radiated energy. Additionally, the single-sideband out-of-band energy, measured above 110 kHz and below 90 kHz, is less than 5% of the total radiated energy [18]. The simulated signal represents a standard eLoran signal, characterized by a sampling frequency of 1 MHz and a data length of 400. The eLoran pulse waveform is determined by the current waveform at the base of the transmit antenna, described by the following expression for the antenna bottom current $i(t)$:

why 65? and why tao<t<tao-65?

$$i(t) = \begin{cases} 0 & t < \tau \\ A(t-\tau)^2 \exp\left[\dfrac{-2(t-\tau)}{65}\right] \cdot \sin(0.2\pi t + pc) & \tau < t < \tau + 65 \end{cases} \quad (1)$$

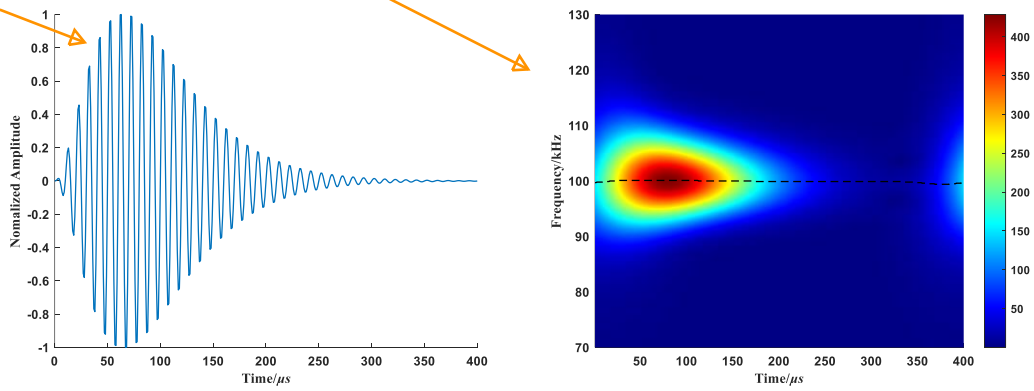
what is the imaginary line?

Where " i(t) " is the antenna current of the eLoran waveform; " A " is the normalization constant (unit A) related to the antenna current peak; " t " is the time (unit μs); " τ " is the envelope to cycle difference（ECD) (unit μs); " pc " is the phase encoding parameter (unit rad).

ECD denotes the temporal shift of the pulse-shaped envelope, defined as the imaginary line connecting the peak of each sinusoidal period, resulting from signal propagation in relation to the standard zero-crossing point of the third period. The displacement of the zero-crossing point of the third period directly influences the magnitude of ECD, as the receiver identifies the correct standard zero-crossing point through the accurate pulse envelope. If ECD is excessively large, it will adversely impact the receiver's ability to recognize the normal period, leading to a significant tracking error in subsequent decoding. To ensure effective signal reception, the transmitting station must maintain the ECD within a specified range. For eLoran monitoring and assessment, peripheral evaluation criteria include a measurement range from -2.5μs to 2.5μs and an accuracy of ⩽1.5μs. The shape of the eLoran pulse and the NTFT spectrum are shown in **Figure 1**, and the dashed line represents the maximum value of the eLoran signal spectrum over time.

how do you get this NTFT plot?

how to get this plot from (1)? or what relation between them?



(**a**) (**b**)

Figure 1. The eLoran normalized waveform and NTFT spectrum:(**a**) eLoran single pulse shape; (**b**) eLoran single pulse NTFT spectrum.

2.2. Research on Adaptive Filtering Algorithm for eLoran Signals

The VSS-LMS algorithm is the most prevalent adaptive filtering method in eLoran signal processing. It effectively addresses the trade-off between convergence speed and steady-state error found in traditional LMS algorithms by dynamically adjusting step size parameters. However, the complexity of the input signal inevitably leads to zero-point drift during processing. This paper employs FIR, IIR, wavelet decomposition, and a segmented inaction algorithm to filter the input signal of the adaptive filtering process [19].

The common variable step LMS algorithm uses the error from the adaptive process as the input parameter and the step size as the output. It incorporates these elements into a corresponding function to establish the relationship between error and step size. According to the definition formula of autocorrelation matrix and cross-correlation vector, it is obtained that LMS algorithm uses the instantaneous estimation of the autocorrelation matrix $\overline{\boldsymbol{R}}$ and instantaneous estimation of cross-correlation vectors $\overline{\boldsymbol{p}}$ [20,21]:

$$\overline{\boldsymbol{R}} = \boldsymbol{x}_n \boldsymbol{x}_n^H \tag{2}$$

$$\overline{\boldsymbol{p}} = \boldsymbol{x}_n d^*(n) \tag{3}$$

$$\boldsymbol{x}_n = \left[x(n)\ x(n-1)\ \ldots\ x(n-\mathrm{N}+1)\right]^T \tag{4}$$

Where "$\overline{\boldsymbol{R}}$ "denotes the instantaneous estimation of the autocorrelation matrix, "$\boldsymbol{x}_n$ "denotes the input signal vector, "H " denotes the conjugate transposition, ,and "$\overline{\boldsymbol{p}}$ " denotes the instantaneous estimation of cross-correlation vectors and "$d^*(n)$ "denotes the conjugate transposition of the expected response signal.

The derivation of the cost function $J(w)$ can be found in reference [22]. The instantaneous state of the gradient vector at this time $\nabla\overline{\boldsymbol{J}}(\mathrm{n})$ is:

$$\nabla\overline{\boldsymbol{J}}(w) = 2\frac{\partial J(w)}{\partial w^*} = 2\boldsymbol{R}\boldsymbol{w}_n - 2\boldsymbol{p} = 2\boldsymbol{x}_n\boldsymbol{x}_n^H\boldsymbol{w}_n - 2\boldsymbol{x}_n d^*(n) = -2\boldsymbol{x}_n e^*(n) \tag{5}$$

$$\boldsymbol{w}_n = \left[w(n)\ w(n-1)\ \ldots\ w(n-\mathrm{N}+1)\right]^T \tag{6}$$

$$e(n) = d(n) - y(n) = d(n) - \boldsymbol{w}_n^H\boldsymbol{x}_n = d(n) - \boldsymbol{x}_n^T\boldsymbol{w}_n^* \tag{7}$$

Where "$\boldsymbol{w}_n$ "denotes the conjugate transpose of the representation weight coefficients. "e "denotes the error of the adaptive filter and "$e^*(n)$ "denotes the conjugate transposition of the error of the adaptive filter.

The updated equation of the weight vector becomes:

$$\boldsymbol{w}_{n+1} = \boldsymbol{w}_n + \mu\boldsymbol{x}_n e^*(n) \tag{8}$$

During the filtering process, neglecting the anticipated signal adjustment introduces gradient noise in the iterative procedure. The weight vector in the LMS algorithm converges toward the optimal solution w_0, and the error associated with the weight vector can be defined as:

$$\boldsymbol{\Delta}_n = \boldsymbol{w}_n - \boldsymbol{w}_0 \tag{9}$$

According to the update equation (8) of the weight vector, the iterative formula for the weight vector error is obtained.

$$\boldsymbol{\Delta}_{n+1} = \boldsymbol{\Delta}_n + \mu\boldsymbol{x}_n e^*(n) \tag{10}$$

By substituting equation (5) into the above formula and simplifying it, we can obtain

$$\boldsymbol{\Delta}_{n+1} = \boldsymbol{\Delta}_n + \mu\boldsymbol{x}_n d^*(n) - \mu\boldsymbol{x}_n\boldsymbol{x}_n^T\boldsymbol{w}_n^* \tag{11}$$

By simultaneously calculating the mathematical expectation of equation (11), we can obtain:

$$E[\boldsymbol{\Delta}_{n+1}] = E[\boldsymbol{\Delta}_n] + \mu E[\boldsymbol{x}_n d^*(n)] - \mu E[\boldsymbol{x}_n\boldsymbol{x}_n^T\boldsymbol{w}_n^*] \tag{12}$$

Since the weight vector is a known vector, equation (12) can ultimately be simplified to:

$$E[\Delta_{n+1}] = (\boldsymbol{I} - \mu \boldsymbol{R}) E[\Delta_n] \quad (13)$$

Where " $\boldsymbol{I}$ " denotes the identity matrix.

When $n \to \infty$, the weight vector error $\Delta_n = 0$, at this time, the mean of the obtained weight vector approaches the optimal weight vector w_0, and the step size factor should satisfy :

$$0 < \mu < \frac{2}{\lambda_{\max}} \quad (14)$$

During filtering, the step-size parameter determines how quickly the estimate converges. Existing approaches typically fix this parameter within a predetermined range, which creates a trade-off: when systematic error is large at the start of processing, rapid convergence is desirable; once the error has diminished, the weight coefficients should oscillate only minimally around the optimum. To reconcile these competing demands, Gao Ying et al. [23] introduced a novel VSS-LMS algorithm that utilizes a step-size update function based on the characteristics of the normal distribution (Gaussian) curve, replacing the traditional sigmoid function. This new algorithm features a smoother peak. By using the mean of the instantaneous error as the independent variable for the normal distribution curve function, the final expression for the step size μ is derived:

$$\mu(n) = \mu_{min} + (\mu_{max} - \mu_{min}) \cdot e^{(-\alpha \cdot | e(n)|^2)} \quad (15)$$

Where " α "denotes the smoothing factor, " μ_{max} "denotes the maximum step size, " μ_{min} "denotes the minimum step size and " $e^{(-\alpha|e(n)|^2)}$ " denotes the interpolation functions which provides smooth transitions.

In this study, the adaptive filtering algorithm utilizes this step size expression as a reference and compares the zero-point drift suppression effects of four primary filtering algorithms on the positive zero crossing point of the third period.

2.3. Zero-Point Drift Suppression Method for Signal Pre-filtering of Traditional Filters

2.3.1 Zero-Point Drift Suppression Method for Signal Pre-filtering Based on FIR/IIR Filters

The eLoran signal primarily concentrates energy in the 90-110 kHz range, necessitating the construction of a band-pass FIR filter with a passband of 90-110 kHz. The Butterworth filter, known for its smooth response and absence of passband ripple, is selected as the prototype IIR filter in this study. The passband is set to 90-110 kHz, while the stopband is defined from 85-115 kHz, ensuring a passband amplitude of 1dB and a stopband amplitude of 60dB.

2.3.2. Zero-Point Drift Suppression Method for Signal Pre-filtering based on Wavelet-decomposition Algorithm

The Dmeyer [15] wavelet selected for reconstructing weak eLoran signals has its decomposition level set to 8. To investigate the impact of various threshold functions on the extraction of weak eLoran signals, we employ soft threshold, hard threshold, and the threshold functions employed in the following five references which are shown in **Table 1.**

Table 1. The hard threshold, soft threshold, and threshold functions utilized in the five references.

Threshold Function	Mathematical Expressions for Each Threshold Function
hard threshold	$y = sign(x) \cdot max\left(\lvert x \rvert - t, 0\right), t$
	$sign(x)$ denotes the sign function
soft threshold	$y = x \cdot \mathbb{I}_{\{\lvert x \rvert > t\}}$, $\mathbb{I}$ denotes the indicator function

Threshold Function	Mathematical Expressions for Each Threshold Function
Reference [24]	$y = sign(x) \cdot max(\sqrt{\lvert x^2 \rvert - t^2}, 0)$
Reference [25]	$y = \begin{cases} sign(x) \cdot \left(\lvert x \rvert - 2^{t-\lvert x \rvert} \right) & \text{if } \lvert x \rvert > t \\ 0 & \text{if } \lvert x \rvert \le t \end{cases}$
Reference [26]	$y = \begin{cases} sign(x) \cdot \left(\lvert x \rvert - \frac{2t}{1+e^{\frac{\lvert x \rvert - t}{t}}} \right) & \text{if } \lvert x \rvert > t \\ 0 & \text{if } \lvert x \rvert \le t \end{cases}$
Reference [27]	$y = \begin{cases} sign(x) \cdot \left(\lvert x \rvert - \frac{t}{1+\alpha} \cdot \gamma^{\sqrt{x^2 - t^2}} \right) & \text{if } \lvert x \rvert > t \\ sign(x) \cdot \frac{\alpha}{1+\alpha} \cdot \left(e^{10\lvert x \rvert - t} \right) \cdot \lvert x \rvert & \text{if } \lvert x \rvert \le t \end{cases}$ α , β denotes the adjustment parameters
Reference [28]	$y = \begin{cases} sign(x) \cdot \left(\lvert x \rvert - \frac{t}{\left[\lvert x \rvert^{\beta} - \lvert t \rvert^{\beta} + 1 \right]^{1/\beta}} \cdot \frac{1}{e^{(\lvert x \rvert - t)^{1/\alpha}}} \right) & \text{if } \lvert x \rvert > t \\ 0 & \text{if } \lvert x \rvert \le t \end{cases}$ α , β denotes the adjustment parameters

how this is shown in figure (1)a?

According to the reference General Technical Conditions for Marine Loran-C Receiving Equipment [29], the SNR of eLoran signals is specifically defined as the ratio of the signal receiving level to the noise level. This ratio can be expressed in either dimensionless numbers or decibels. The eLoran signal receiving level is defined as the effective value of the continuous wave at the 25 μs point, measured from the pulse envelope line. Its valid value, E, is defined as:

$$E = \frac{env(25)}{\sqrt{2}} \tag{16}$$

where" $env(25)$ "denotes the 25 μs point level at the onset of the eLoran pulse envelope.

To identify the most appropriate wavelet threshold function for fusion with adaptive filtering, this simulation was conducted by introducing random noise at a SNR of -30dB.

Table 2. Signal reconstruction performance indicators under different threshold functions.

Threshold Function	**RMSE**	**NCC/%**	**Zero-Point Drift Value/** μs
hard threshold	0.34879	0.56799	0.65574
soft threshold	0.31009	0.63553	0.47756
Reference [24]	0.22790	0.78673	0.87972
Reference [25]	0.21187	0.80981	0.46794
Reference [26]	0.20670	0.82391	0.40962
Reference [27]	0.24872	0.76990	0.49850
Reference [28]	**0.12605**	**0.93093**	**0.34900**

The performance indicators for wavelet decomposition (WD) simulation using various threshold functions are presented in the **Table 2**. After evaluating the accuracy of the reconstructed signal waveform through the RMSE, normalized correlation coefficient (NCC), and zero-point drift value, the threshold function proposed in references [28] is chosen for the wavelet decomposition algorithm examined in this study.

2.4. Zero-Point Drift Suppression Method for Signal Pre-filtering Based on Inaction Method

Generally, for a complex time signal $f(t) \in C$, its linear time-frequency transform can be expressed as[30,31]:

$$\Psi f(\tau,\varpi) = \int_R f(t)\overline{\psi}(t-\tau,\varpi)\mathrm{d}t, \quad \tau,\varpi \in R \tag{17}$$

"τ" denotes the time parameter,"ϖ" denotes the frequency parameter, the dash line "-" denotes the conjugation, "$\psi(t,\varpi)$" denotes the kernel function, "R" denotes the real domain.

Fourier transform of kernel function $\Psi(t,\varpi)$ of normal time-frequency transform can be expressed as:

$$\hat{\psi}(\omega,\varpi) = \int_R \psi(t,\varpi)\exp(-\mathrm{j}\omega t)\mathrm{d}t \neq 0 \tag{18}$$

The following two conditions are met:

(1) $\hat{\psi}(\omega,\varpi) = 1$, when $\omega = \varpi$;

(2) $|\hat{\psi}(\omega,\varpi)| < 1$, when $\omega \neq \varpi$.

Where"$|\ |$"denotes modulo, "j" denotes imaginary, "$\wedge$"denotes Fourier transform operator, and "$\cdot$" denotes almost everywhere.

The kernel function used in this paper is:

$$\psi(t,\varpi) = |\mu(\varpi)| \cdot w(\mu(\varpi)t) \cdot \exp(\mathrm{j}\varpi t), (\mu(\varpi) \in R) \neq 0 \tag{19}$$

Where "$w(t)$" is the window function and "$\mu(\varpi)$" is a real function, which can be called a time-frequency resolution adjuster.

In the kernel function, varying the values or expressions for $\mu(\varpi)$ and the window function $w(t)$ can produce distinct time-frequency transformations. When $\mu(\varpi) = 1$, the NTFT corresponds to a normal Gabor transformation. This paper focuses on eLoran signals, and the NTFT kernel function constructed herein represents the normal wavelet transform. The kernel function for this normal wavelet transform must satisfy the following conditions:

$$\begin{cases} \mu(\varpi) = \varpi \\ w(\mathrm{t}) = \dfrac{1}{\sqrt{2\pi\sigma}}\exp(-\dfrac{\mathrm{t}^2}{2\sigma^2}), \sigma > 0 \end{cases} \tag{20}$$

Where "σ" indicates the Gaussian window width parameter.

Therefore, the kernel function constructed in this paper is:

$$\psi(t,\varpi) = \frac{|\varpi|}{\sqrt{2\pi\sigma}}\exp(-\frac{(\varpi t)^2}{2\sigma^2} + \mathrm{j}\varpi t) \tag{21}$$

Substitute equation **(21)** to construct the standard wavelet transform:

$$\Psi f(\tau,\varpi) = \frac{|\varpi|}{\sqrt{2\pi\sigma}}\int_R f(t)\exp(-\frac{\varpi^2(t-\tau)^2}{2\sigma^2} + \mathrm{j}\varpi(\tau - t))\mathrm{d}t, \quad \tau,\varpi \in R \tag{22}$$

Suppose the harmonic signal $f(\mathrm{t})$ is:

$$f(t) = \mathrm{A}\sin(2\pi f t + \varphi) \tag{23}$$

According to Euler's formula $\sin\theta = (\mathrm{e}^{\mathrm{j}\theta} - \mathrm{e}^{-\mathrm{j}\theta})/2\mathrm{j}$, it is expanded into the sum of two complex exponential signals:

$$f(t) = \frac{\mathrm{A}}{2\mathrm{j}}\exp(\mathrm{j}(2\pi f t + \varphi)) - \frac{\mathrm{A}}{2\mathrm{j}}\exp(-\mathrm{j}(2\pi f t + \varphi)) \tag{24}$$

Let $\mathrm{A}_1 = \frac{\mathrm{A}}{2\mathrm{j}}\exp(\mathrm{j}\varphi)$, $\mathrm{A}_2 = -\frac{\mathrm{A}}{2\mathrm{j}}\exp(-\mathrm{j}\varphi)$, $\beta = 2\pi f$, The equation **(24)** becomes:

$$f(t) = \mathrm{A}_1\exp(\mathrm{j}\beta t) + \mathrm{A}_2\exp(-\mathrm{j}\beta t) \tag{25}$$

Substituting equation **(25)** into the kernel function defined in equation **(17)**, the normal time-frequency transform $\Psi f(\mathrm{t})$ as follows:

$$\begin{aligned}\Psi f(t) &= \int_R (\mathrm{A}_1 \exp(\mathrm{j}\beta t) + \mathrm{A}_2 \exp(-\mathrm{j}\beta t)) \cdot \bar{\Psi}(t-\tau,\varpi)\mathrm{d}t \\ &= \int_R (\mathrm{A}_1 \exp(\mathrm{j}\beta t) + \mathrm{A}_2 \exp(-\mathrm{j}\beta t)) \cdot |\mu(\varpi)| \cdot w(\mu(\varpi)(t-\tau)) \cdot \exp(-\mathrm{j}\varpi(t-\tau))\mathrm{d}t\end{aligned} \quad (26)$$

Let $t-\tau = x, t = x+\tau$, substitute into (26), the normal time-frequency transform $\Psi f(\mathrm{t})$ becomes:

$$\begin{aligned}\Psi f(t) = \mathrm{A}_1 |\mu(\varpi)| \exp(\mathrm{j}\beta\tau) \int_R (\exp(-\mathrm{j}(\varpi-\beta)x) \cdot w(\mu(\varpi)x)dx + \\ \mathrm{A}_2 |\mu(\varpi)| \exp(-\mathrm{j}\beta\tau) \int_R (\exp(-\mathrm{j}(\beta+\varpi)x) \cdot w(\mu(\varpi)x)dx\end{aligned} \quad (27)$$

Combined index terms, let $\Psi f(\mathrm{t})$ be the sum of two subfunctions, and the equation becomes:

$$\Psi f(\mathrm{t}) = \Psi f_1(\mathrm{t}) + \Psi f_2(\mathrm{t}) \quad (28)$$

Since $f_1(\mathrm{t})$ and $f_2(\mathrm{t})$ are derived the same, only is derived below.

From Fourier scaling: $\mathrm{F}_{t-\omega} f(\alpha t) = \frac{1}{|\alpha|} \mathrm{F}(\mathrm{j}\frac{\omega}{\alpha})$, let $\nu = \mu(\varpi)x$, $dx = \frac{dv}{\mu(\varpi)}$ substitute into $\Psi f_1(\mathrm{t})$ gives:

$$\Psi f_1(\tau,\varpi) = \mathrm{A}_1 \exp(\mathrm{j}\beta\tau) \int_R w(v) \exp(-\mathrm{j}\frac{(\varpi-\beta)}{\mu(\varpi)}\varpi)dv \quad (29)$$

Similarly, the normal time-frequency transform of $\Psi f_2(\mathrm{t})$ is:

$$\Psi f_2(\tau,\varpi) = \mathrm{A}_2 \exp(-\mathrm{j}\beta\tau) \int_R w(v) \exp(-\mathrm{j}\frac{(\varpi+\beta)}{\mu(\varpi)}\varpi)dv \quad (30)$$

The integral term in the equation represents the Fourier transform of the expanded window function. According to Equation **(30)**, it can be obtained that:

$$\Psi f(\tau,\varpi) = \mathrm{A}_1 \exp(\mathrm{j}\beta\tau)\hat{w}(\frac{\varpi-\beta}{\mu(\varpi)}) + \mathrm{A}_2 \exp(-\mathrm{j}\beta\tau)\hat{w}(\frac{\varpi+\beta}{\mu(\varpi)}) \quad (31)$$

In the equation, "$\wedge$" denotes the Fourier transform.

Therefore, the NTFT spectrum of the harmonic signal is expressed as:

$$|\Psi f(\tau,\varpi)| = \left|\mathrm{A}_1 \exp(\mathrm{j}\beta\tau)\hat{w}(\frac{\varpi-\beta}{\mu(\varpi)}) + \mathrm{A}_2 \exp(-\mathrm{j}\beta\tau)\hat{w}(\frac{\varpi+\beta}{\mu(\varpi)})\right| \quad (32)$$

It can be seen that when $\varpi = \beta$, $\varpi = -\beta$, the NTFT property of formula **(32)** that NTFT spectrum attains a maximum value, indicating that the NTFT spectrum can determine the frequency components of narrowband interference signals without bias.

$$\begin{aligned}|\Psi f(\tau,\varpi)| = \mathrm{Maximum} \Leftrightarrow \varpi = \beta, \forall\tau \in \mathrm{R} \\ \Psi f(\tau,\varpi) = f(\tau) = \mathrm{A}\exp(\mathrm{i}(\beta t + \varphi)) \Leftrightarrow \forall\tau \in \mathrm{R}\end{aligned} \quad (33)$$

When $\hat{\mathrm{w}}(\varpi)$ takes a maximum value of 1, then:

$$\Psi f(\tau,\varpi) = \Psi f_1(\tau,\varpi) + \Psi f_2(\tau,\varpi) = \mathrm{A}\sin(2\pi f t + \varphi) \quad (34)$$

Formula **(34)** shows that NTFT enables unbiased instantaneous amplitude and phase analysis. The coefficients extracted along the ridge lines of the NTFT spectrum represent the signal itself. This extraction technique is termed the inaction method, which functions as a line-pass filter. Compared to traditional FIR/IIR band-pass filtering methods, the inaction method offers greater noise immunity and robustness. Additionally, it effectively suppresses zero-point drift phenomena and enhances positioning accuracy. The initial frequency domain filtering process of segmented inaction method is shown in **Figure 2**.

please add more deatil words on how to read the Figure 2, linked with above equations

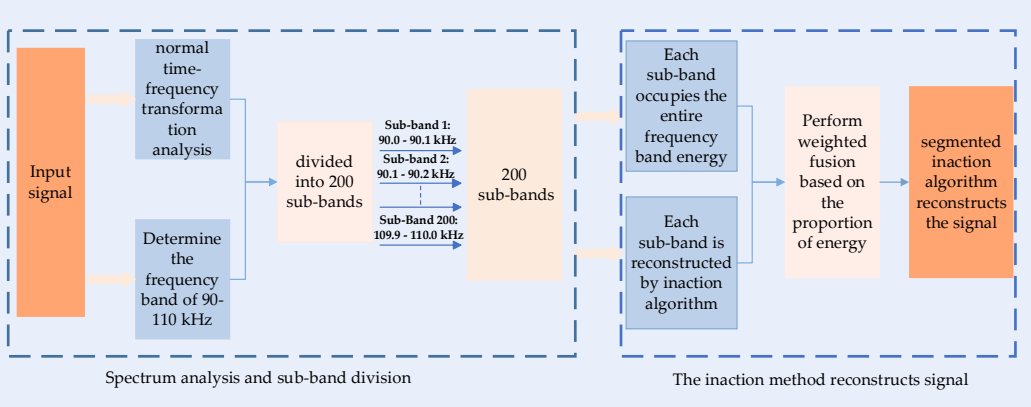


Figure 2. Flow chart of segmented inaction algorithm.

2.4.2. Selection of Window Function Length

Signal accuracy evaluation primarily relies on the RMSE, with the NCC serving as a supplementary measure. The definitions of RMSE and NCC are provided below. Additionally, performance indicators for subsequent simulations and measured data include the correlation coefficient (R) and the definition of R-RMSE. R-RMSE is defined as the ratio of RMSE to the average amplitude of the simulation waveform data. In subsequent simulations and actual measurements, using RMSE alone does not adequately convey relative accuracy. Therefore, the implementation of R-RMSE provides a more intuitive assessment of the prediction results quality.

$$RMSE = \sqrt{\frac{\sum_{i=1}^{N}(a_i - b_i)}{N}} \quad (35)$$

$$NCC = \frac{\sum_{n=1}^{N} A_s(n)A_d(n)}{\sqrt{\left(\sum_{n=1}^{N} A_s^2(n)\right)\left(\sum_{n=1}^{N} A_d^2(n)\right)}} \quad (36)$$

$$R = \frac{\sum_{i=1}^{N}(a_i - \bar{a})(b_i - \bar{b})}{\sqrt{\sum_{i=1}^{N}(a_i - \bar{a})^2 \sum_{i=1}^{N}(b_i - \bar{b})^2}} \quad (37)$$

$$R\text{-}RMSE = \frac{RMSE}{A} \quad (38)$$

Where " a_i "and" b_i "denote the amplitude of the original waveform and filtered waveform, " $\bar{a}$ "and" $\bar{b}$ " denote the average of the original waveform and filtered waveform. " N " denote the length of the data, " A " denote the average value of the original waveform amplitude." A_s "denotes the original waveform and" A_d "denotes the filtered signal. Using RMSE alone does not adequately convey relative accuracy.

When conducting normal time-frequency transformations on a finite-length time series, the window function becomes incomplete during certain intervals at both the beginning and the end of the data. This incompleteness results in the unavailability of NTFT coefficients for these edge periods, leading to inaccuracies in signal extraction at the data's boundaries. The extent of this edge effect is contingent upon the length of the window function. Consequently, this paper employs a standard Gaussian window with an infinite boundary approaching zero. Additionally, due to the inadequate signal reconstruction performance of the single inaction algorithm under low signal-to-noise ratio conditions, a simulation is performed to determine a more suitable window function length. This simulation incorporates -5 dB of random noise, with a sampling rate set at 1MHz. **Figure 3**

illustrates the original and reconstructed signals corresponding to different window lengths.

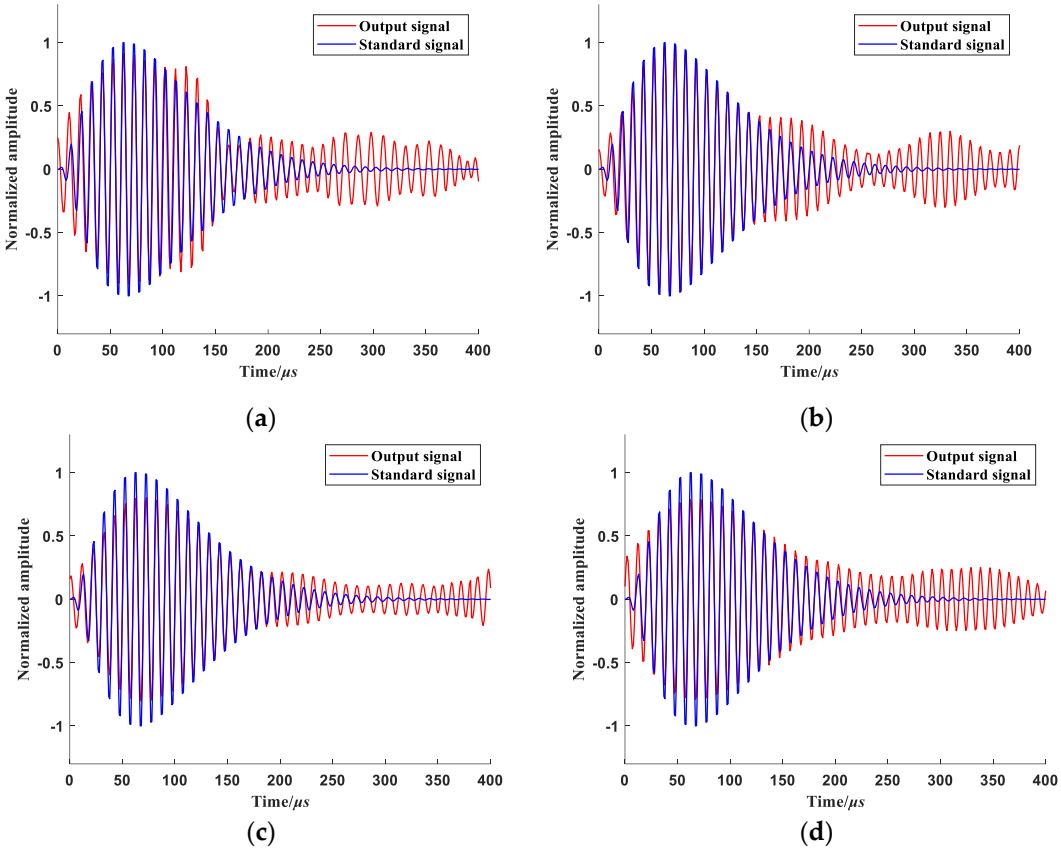


Figure 3. Inaction method reconstructed signal waveform and original signal waveform under different window lengths:(a) window lengths 50; (b) window lengths 80; (c) window lengths 100; (d) window lengths 120.

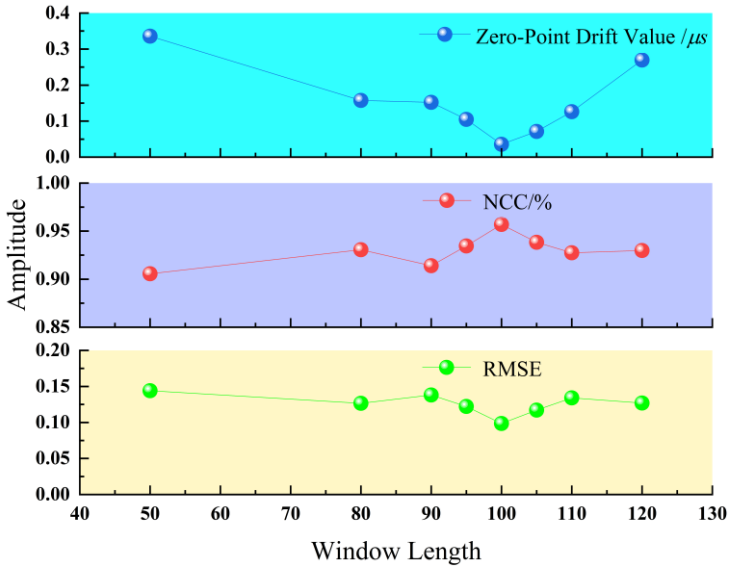


Figure 4. Comparison of the evaluation of different window function length conditions.

The evaluation of the optimal window function length for the waveform precision of the output eLoran reconstructed signal and the original signal is based on the RMSE, signal R, and R-RMSE values. **Figure 4** illustrates that when the window length is less than

50, the distortion of the reconstructed waveform is more pronounced. As the window length increases, the edge effect length of the inaction algorithm also increases, resulting in greater data loss. When the window length exceeds 120, a peak value emerges, leading to intensified waveform distortion in the first and last segments of the reconstructed signal. To balance waveform distortion and reconstruction accuracy, the optimal window function length should be between 80 and 120. In this study, a window function length of 100 is selected.

3. Simulation Analysis of Zero-Point Drift Suppression

what of these freq bandwidth?

Multi-narrowband frequency?

To evaluate the effectiveness of four combined filtering algorithms in suppressing zero-point drift and enhancing reconstruction accuracy under low SNR conditions, a standard eLoran group signal was generated using MATLAB. This signal was subjected to multi-frequency narrowband interference and band-limited random noise, both at an SNR of -30 dB, with noise frequencies of 87.5 kHz, 92.5 kHz, 97.5 kHz, and 105.5 kHz.

what means noise frequency? why pick these frequencies?

For multi-frequency narrowband interference, which is a form of continuous wave interference, characterized by various artificial radio frequency sources that possess sufficient energy to adversely affect eLoran receiver equipment. This type of interference is representative of real-world scenarios encountered during measurement experiments. Based on the eLoran frequency band range, it can be categorized into synchronous interference, near-synchronous interference, and asynchronous interference. Synchronous interference pertains to signals with carrier frequencies within the 90-110 kHz band, whereas near-synchronous interference involves carrier frequencies within the 70-90 kHz and 110-130 kHz bands. Asynchronous interference is defined as interference with carrier frequencies either below 70 kHz or above 130 kHz. This paper primarily focuses on simulating near-synchronous and synchronous interference for experimental purposes. The $f_1(t)$ is defined by the following formula:

$$f_1(t) = (env(25) / (10\,\wedge^{SNR_i/20})) \cdot \sin(2\pi \cdot f_i \cdot t) \quad (39)$$

Where " $env(25)$ "denotes the effective value of the continuous-wave component measured at the 25μs level following the line of the eLoran signal pulse envelope. " SNR_i "denotes the signal-to-noise ratio and " f_i "denotes the frequency of the added narrowband interference.

any reasons of pick these waveforms?

can you discuss how this setting is close to real scenarios?

For band-limited random noise, the $f_2(t)$ is defined by the following formula:

$$f_2 = \frac{R_f}{\sqrt{1/N \cdot \sum_{I=1}^{N} R_f \cdot 2.5}} \cdot \left(max(y_0) \cdot 0.505 / \sqrt{2} \right) / \left(10^{(SNR/20)} \right) \quad (40)$$

Where " R_f "denotes the band-limited random noise obtained when Gaussian white noise is passed through an FIR bandpass filter (70 –130 kHz). " SNR "denotes the SNR and " y_0 "denotes the standard eLoran signal.

The simulation signal consists of narrowband interference of four frequencies and band-limited random noise. A combined algorithm combining the four methods with VSS-LMS adaptive filtering was employed for waveform reconstruction. **Figure 5** presents the normalized output waveform alongside the standard eLoran signal waveform after adaptive filtering at -30 dB SNR. At this SNR level, the original signal was completely obscured by noise.

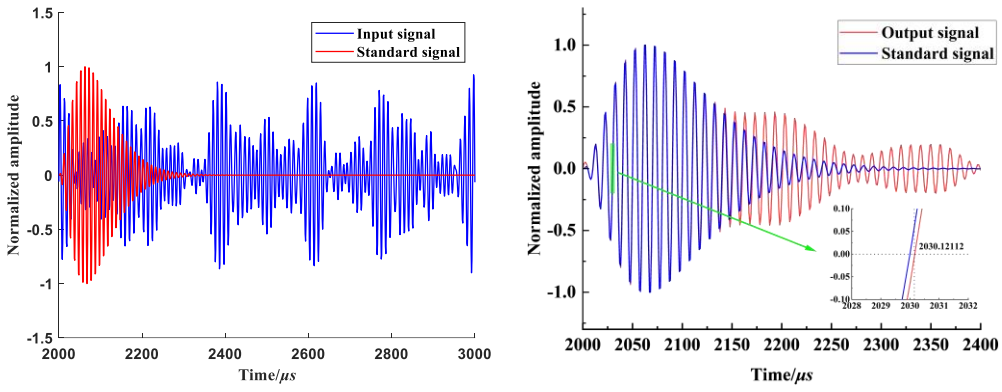


Figure 5. -30dB SNR condition and the normalized output signal and standard signal after adaptive filtering :(**a**) Output signal and standard signal under -30dB SNR condition; (**b**) Output signal and standard signal after adaptive filtering.

Figure 6 illustrates the filtering performance of the four combined filtering algorithms under the target condition. The waveforms produced by the three conventional filters exhibit significant distortion in this context. In contrast, the segmented inaction method combined adaptive filtering algorithm presented in this study demonstrates notable improvements in waveform fidelity and zero-point drift suppression. However, a limitation of this approach is that the recovered waveform still displays some fluctuations at the tail. This issue arises from the inherent edge effect of the window function, with the amplitude of these fluctuations increasing as the SNR decreases.

All of your wave plots are shown as normalized outputs.

Can you clarify what they are normalized to?

I suggest instead defining a similarity function between the filtered signal and the standard signal, specifically in the region in the block.

Since the main concern is the correctness of the zero-crossings, the similarity measure should emphasize that aspect.

Whether other parts of the waveform match or not is less important.

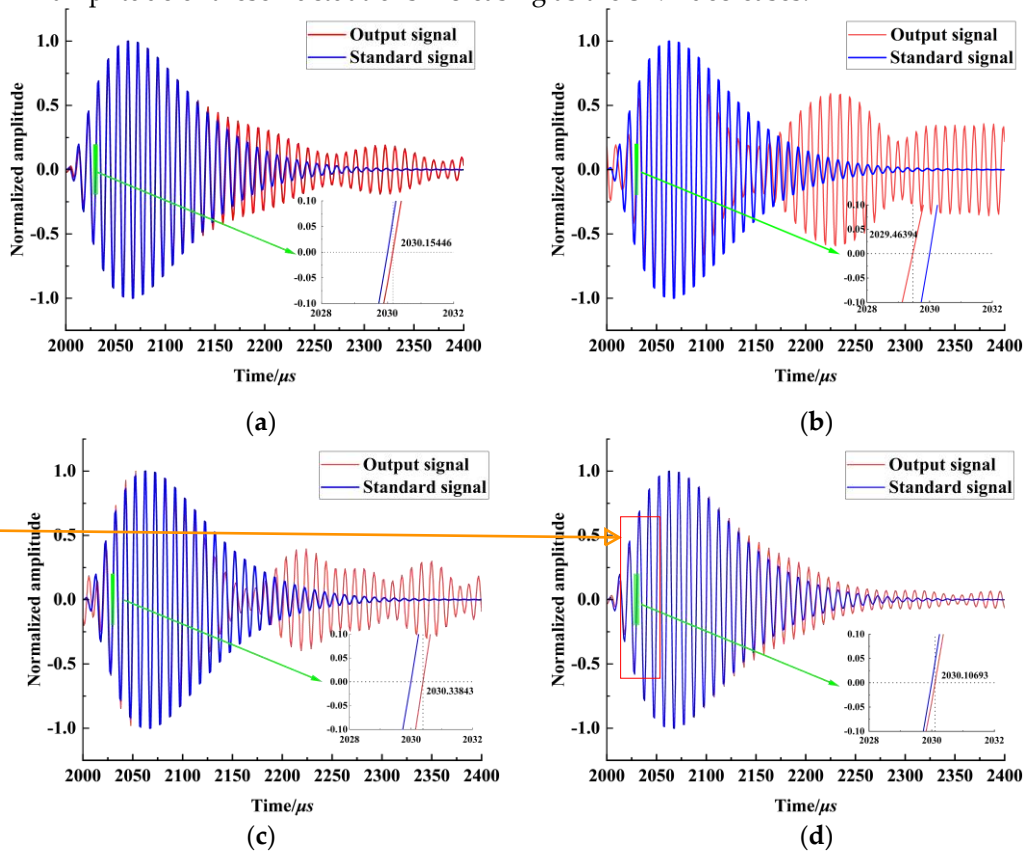


Figure 6. Normalized output signals and standard signals of different combined filtering algorithms under target conditions :(**a**) FIR+VSS-LMS; (**b**) IIR+VSS-LMS; (**c**) WD +VSS-LMS; (**d**) Inaction +VSS-LMS.

The RMSE, R-RMSE, and positive zero-crossing point drift of the third cycle are calculated using the first 400 μs eLoran single pulse signals under the target condition. The **Figure 6** simulation results indicate that the segmented inaction method combined adaptive filtering algorithm enhances filtering accuracy compared to the single adaptive filtering algorithm. This improvement is particularly notable for the zero-crossing point drift phenomenon observed in the third cycle.

Table 3. Performance indicators of signal reconstruction by four combined filtering and single adaptive Filtering methods.

Combined Method	Performance indicators			
	RMSE	R	R-RMSE	Zero-Point Drift Value/μs
VSS-LMS	0.12112	0.85612	0.62463	0.16459
FIR+ VSS-LMS	0.09435	0.89364	0.48660	0.15446
IIR+ VSS-LMS	0.24770	0.61694	1.27742	0.53606
WD+ VSS-LMS	0.15426	0.74983	0.79555	0.38843
Inaction +VSS-LMS	**0.05554**	**0.87371**	**0.28642**	**0.10693**

Table 3 demonstrates that the output signal of the segmented inaction method combined algorithm presented in this paper has a RMSE that is 54.1% lower and a R-RMSE that is 54.1% lower than that of the single adaptive algorithm. Additionally, the similarity between the output signal and the original waveform is greater. In contrast, the other three common filters exhibit poor compatibility in combined, resulting in suboptimal signal reconstruction. Notably, the proposed method presented here corrects the zero-point offset by 35% and significantly reduces phase distortion. This has substantial implications for enhancing the positioning accuracy of eLoran and for period identification.

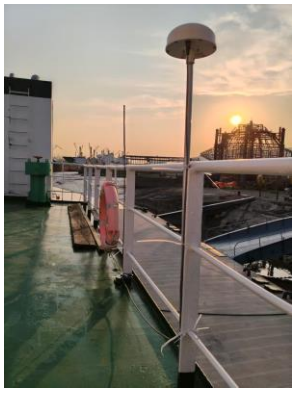
4. Experimental verification

4.1. Experimental and time-frequency domain analysis of eLoran signals

To assess the effectiveness of the segmented inaction method combined with the adaptive filtering algorithm in correcting the zero-point drift of the standard zero-crossing point in the third period of the eLoran signal, we conducted an eLoran front-end digital signal acquisition experiment. Data collection occurred at two locations: a coastal port and an inland city. The coastal port data was collected at 15:31:07 on June 13, 2024, with a sampling rate of 3.2 MHz and a SNR of -18dB. In contrast, the inland city data was collected at 09:17:28 on April 3, 2025, with a sampling rate of 1.6 MHz and a SNR of 14dB. **Figure 7** presents the schematic diagrams of the equipment used in both tests.



(**a**)



(**b**)



(**c**)

Figure 7. Magnetic antennas and electrical antennas from two experiments: (**a**) Electrical antenna for the coastal experiment; (**b**) Magnetic antenna for the coastal experiment;(**c**) Magnetic antenna for inland city experiment.

Figure 8 presents the digital signals from the eLoran front end collected during the two experiments. Given the extensive length of the data, one segment from each of the two collected digital signals was analyzed. The signals intercepted from coastal ports exhibit significant interference due to environmental obstructions, resulting in a relatively low SNR. Analysis of the single-pulse waveform reveals noticeable distortion, which can lead to errors in period discrimination. To facilitate signal analysis, amplitude compensation was applied to the front-end digital signals collected from coastal ports. In contrast, the signals intercepted in inland cities demonstrate a relatively high SNR. Their waveforms more closely resemble standard signals, attributed to reduced environmental obstructions and interference.

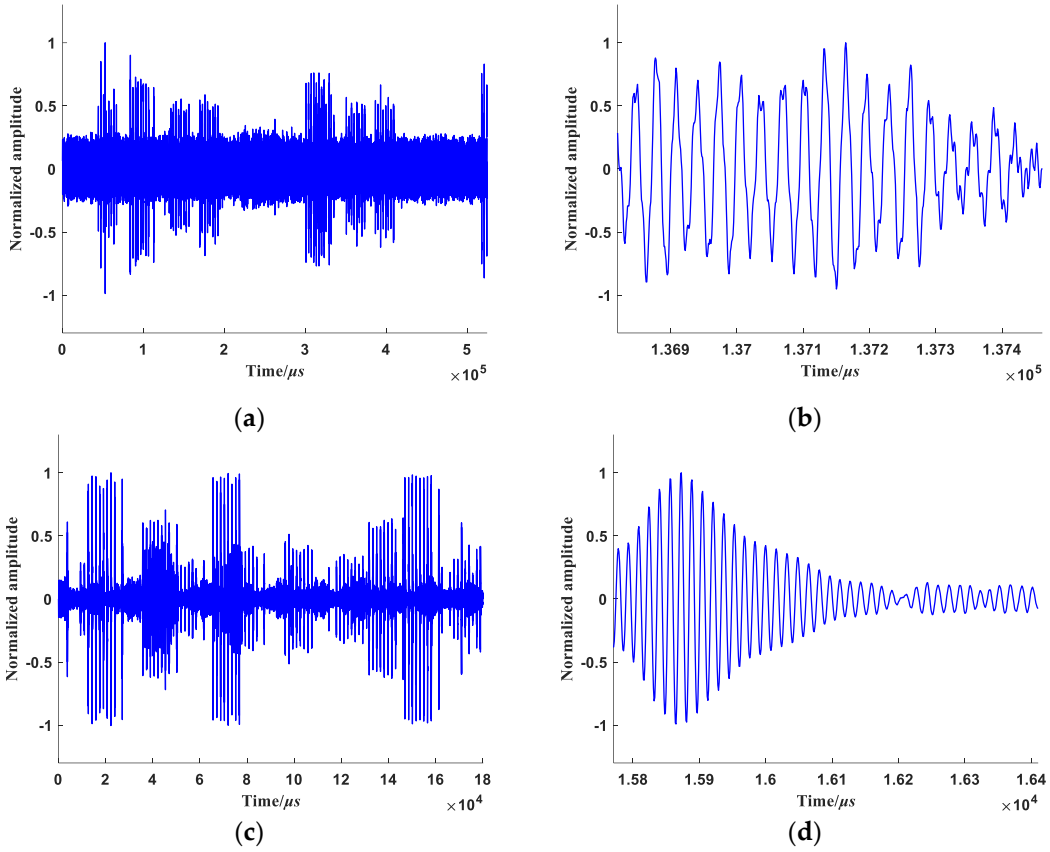


Figure 8. Normalized waveform amplitudes of the eLoran front-end digital signals collected from two locations and the normalized waveform amplitudes of the eLoran single pulses: (**a**) Normalized waveform amplitude of eLoran signals obtained from coastal ports; (**b**) Normalized waveform amplitude of eLoran single pulses obtained from coastal ports; (**c**) Normalized waveform amplitude of eLoran signals obtained from inland cities; (**d**) Normalized waveform amplitude of eLoran single pulses obtained from inland cities.

4.2. Reconstruction of Measured eLoran signals

Four combined filtering methods are adopted to reconstruct the digital signals of the eLoran front-end collected from two locations. The simulation results for the measured coastal data are presented in **Figure 9,** while the results for the measured data from inland city are shown in **Figure 10**.

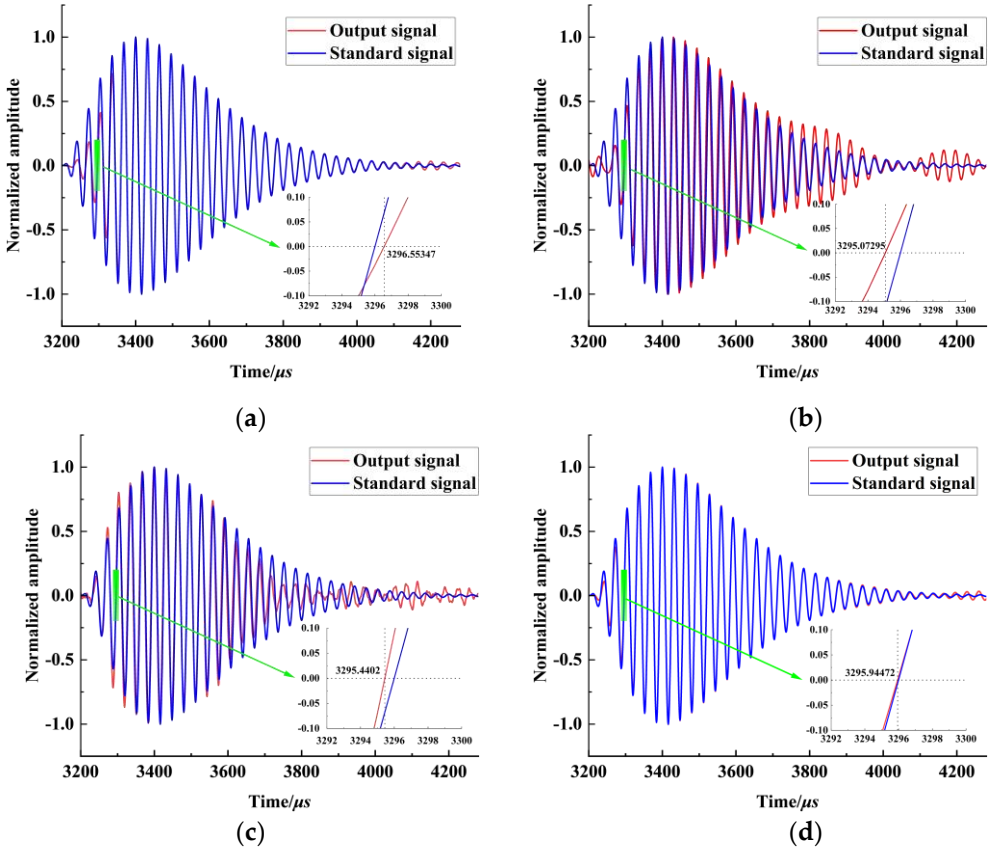


Figure 9. Normalized output signal and standard signal from data collected along the coast using various combined filtering algorithms: (**a**) FIR+VSS-LMS; (**b**) IIR+VSS-LMS; (**c**) WD +VSS-LMS; (**d**) Inaction +VSS-LMS.

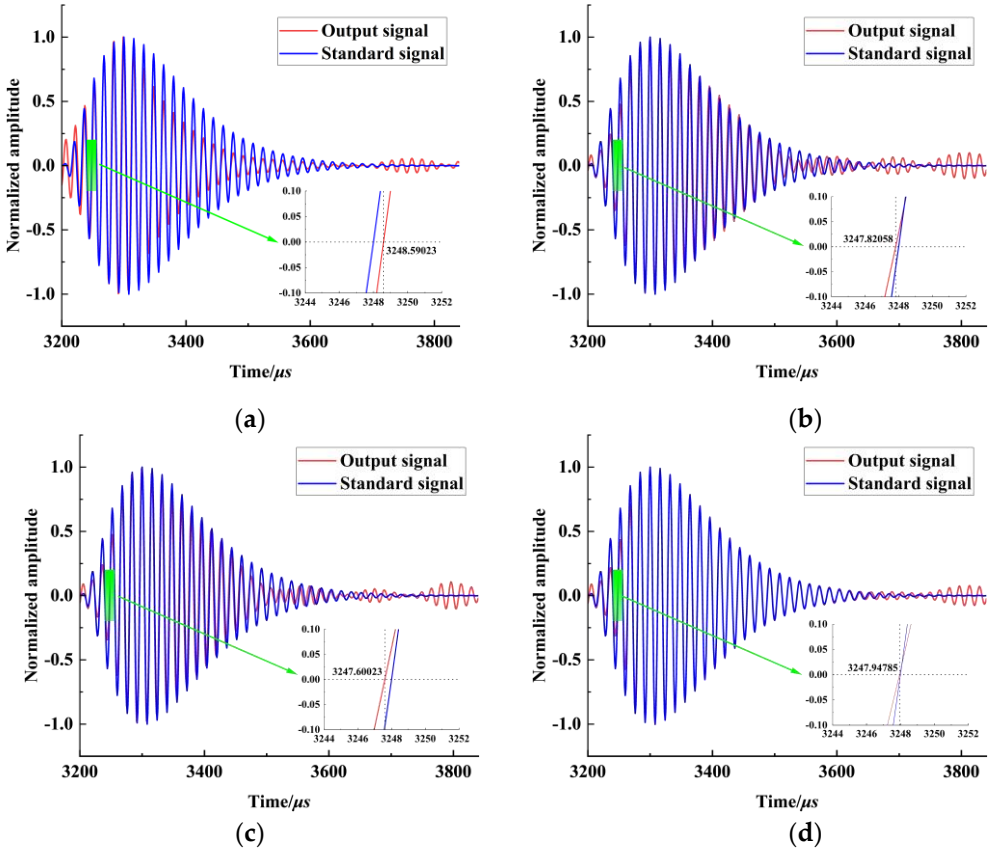


Figure 10. Normalized output signal and standard signal from inland data collected under various combined filtering algorithms: (**a**) FIR+VSS-LMS; (**b**) IIR+VSS-LMS; (**c**) WD +VSS-LMS; (**d**) Inaction +VSS-LMS.

Table 4. Shows the performance indicators of signals reconstructed by four combined filtering algorithms based on the experimental data.

Experimental site	Combined method	Performance indicators			
		RMSE	R/%	R-RMSE	Zero-Point Drift Value/μs
coastland	VSS-LMS	0.02529	0.94800	0.13273	0.26554
	FIR+ VSS-LMS	0.05058	0.94737	0.26542	0.55347
	IIR+ VSS-LMS	0.14773	0.77943	0.77529	0.92705
	WD+ VSS-LMS	0.09776	0.72361	0.51306	0.55973
	Inaction +VSS-LMS	**0.01540**	**0.97680**	**0.08083**	**0.05528**
inland	VSS-LMS	0.05028	0.92656	0.26665	0.11672
	FIR+ VSS-LMS	0.10470	0.90690	0.55525	0.59023
	IIR+ VSS-LMS	0.09553	0.78617	0.50663	0.17942
	WD+ VSS-LMS	0.10518	0.77726	0.55780	0.39977
	Inaction +VSS-LMS	**0.04780**	**0.94201**	**0.25349**	**0.05215**

The performance indicators of the four combined filtering algorithms presented in **Table 4** demonstrate that the algorithm proposed in this paper excels in RMSE, R, R-RMSE, and suppression of zero-point drift. This algorithm shows significant improvements in signal reconstruction compared to traditional combination algorithms. In coastal cities, experimental data indicate that the RMSE of the combined algorithm is 33.3% higher than that of the single VSS-LMS method. Additionally, the correlation coefficient R shows slight improvement, while R-RMSE decreases by 39.1%. Furthermore, the algorithm corrects 79.3% of the zero-point drift and maintains the lead zero-crossing error at a very low level during the third week.

In inland cities, the reduced surrounding occlusion and higher SNR enable a single VSS-LMS algorithm to achieve effective filtering. Experimental data indicate that the combined algorithm proposed in this paper shows only slight improvements in the performance indicators of RMSE, R, and R-RMSE compared to the single VSS-LMS method. However, it compensates for 55.3% of the zero-point drift observed in the third period and maintains a low lead zero-passing error during the third week.

Comparative experiments conducted in two locations demonstrate the filtering stability of the combined algorithm in low SNR environments. It effectively addresses the zero-point drift issue of the single VSS-LMS adaptive filter across varying SNR conditions and outperforms other combined algorithms.

Analysis of the table data reveals significant technical deficiencies in traditional combined algorithms. The FIR combined VSS-LMS algorithm exhibits unstable performance, with deteriorated RMSE and increased R-RMSE. Additionally, signal correlation is markedly reduced, and its correction for the positive zero-crossing in the third period is notably weaker than that of the combined algorithm proposed in this paper. The IIR combined VSS-LMS algorithm suffers from severe phase distortion. The nonlinear phase characteristics of the IIR filter result in considerable waveform distortion, exacerbating the drift of the positive zero-crossing point in the third period. Consequently, it is unsuitable as the initial filter for correction. Furthermore, the WD combined VSS-LMS algorithm demonstrates a negative synergistic effect when combined with the VSS-LMS algorithm due to

the loss of effective signal bandwidth during the small decomposition process. This results in minimal filtering accuracy and inadequate zero-point drift compensation.

Through a comprehensive comparison, the segmented inaction algorithm proposed in this paper offers a superior input environment for the subsequent VSS-LMS algorithm across various environmental conditions. Notably, in low SNR settings, it demonstrates significant improvements compared to three other combined filtering methods. This combined algorithm addresses the zero-point drift phenomenon of the forward zero-crossing point in the third period of the eLoran signal. As a result, the eLoran receiver can achieve more accurate tracking of this point through the phase-locking loop during pulse measurement, leading to higher precision in time difference measurement. By correcting zero-point drift, the algorithm substantially reduces the measurement reference deviation of the pulse, thereby enhancing the reliability of the receiver's period recognition. This improvement significantly decreases the likelihood of period discrimination errors and phase tracking mis-cycles, ultimately enhancing positioning accuracy.

5. Conclusions

this is too long. suggest add a "discussion" section, and make conclusion on your contribution.

This paper analyzes the time-frequency domain characteristics of eLoran and proposes a spectral analysis method for eLoran signals based on NTFT. Meanwhile, a segmented inaction method based on this theory is used to conduct a simulation study on the interference suppression algorithm for eLoran signals. The simulation experiments prove that this joint method significantly suppresses the zero-point drift phenomenon of the third period forward zero-crossing caused by adaptive filtering. Finally, based on the validity verification of the measured signal algorithm in coastal and inland areas, the results prove the superiority of this combined method in signal reconstruction and zero-point drift suppression under strong interference and low SNR conditions. Under different SNR conditions, the zero-point error at the zero-crossing point in the third week is controlled at an extremely low level. The following conclusions are drawn by comparing four filtering methods:

(1) The FIR filter specifically targets the removal of out-of-band noise within the eLoran band while preserving in-band noise. This approach results in unstable signal filtering performance, which does not enhance the subsequent VSS-LMS processing. Consequently, the final signal reconstruction is inferior to that achieved by a standalone VSS-LMS algorithm, and it exacerbates the zero-point drift phenomenon of the eLoran signal.

(2) The IIR filters exhibit an inherent nonlinear phase that causes time delays at specific frequencies within the signal, resulting in significant waveform distortions. The VSS-LMS algorithm cannot correct for this deterministic distortion introduced during preprocessing. Instead, it converges incorrectly on the distortion, leading to performance degradation, particularly in zero-point drift.

(3) The wavelet decomposition combined algorithm is not well-suited for the VSS-LMS algorithm regarding primary filtering. This mismatch leads to considerable waveform distortion and increased error. Additionally, it filters out effective frequency band components in the signal, compromising the original structure of the eLoran signal. Consequently, a "negative synergy" effect arises, exacerbating the zero-point drift phenomenon.

(4) The segmented inaction algorithm presented in this paper serves as an innovative primary filtering method. It effectively retains the useful frequency bands of eLoran signals while filtering out both in-band and out-of-band noise. Additionally, this algorithm demonstrates excellent compatibility and synergy with the VSS-LMS algorithm. The VSS-LMS algorithm minimizes zero-point drift caused by adaptive filtering to an extremely low level. This combination holds significant value and promising applications in engineering.

(5) The inaction algorithm and the VSS-LMS algorithm, through innovative fusion technology, effectively mitigate the zero-point drift issue prevalent in traditional adaptive algorithms within complex environments. In the context of strong interference and low SNRs at coastal ports, this joint algorithm outperforms the standalone VSS-LMS algorithm, achieving a 33.3% improvement in RMSE, a 39.1% enhancement in R-RMSE, a 79.3% correction of zero-point drift, and maintaining the zero-crossing error at an exceptionally low level during the third week. In inland environments characterized by weak interference and high SNRs, other performance metrics have shown modest improvements, with zero-point drift corrected by 55.3%. Experiments conducted in two distinct locations have convincingly demonstrated that the combined algorithm possesses exceptional environmental adaptability and robustness, effectively suppressing various interferences and providing a reliable technical foundation for high-precision timing and period identification.

All experimental data presented in this paper were collected under favorable weather conditions, thus excluding the sharp pulse interference within the frequency bandwidth of the eLoran signal that severe thunderstorms can produce. Future research will concentrate on enhancing the operational efficiency of this joint algorithm and mitigating extreme in-band noise generated by thunderstorms. Strong pulse interference may hinder the eLoran receiver's ability to accurately track the forward zero-crossing point of the third period in the phase-locked loop during pulse measurement, which can lead to increased time difference measurement deviation and diminished reliability in period recognition. Additionally, this interference will expand the applicable boundaries of the joint filtering method, facilitating the separation of interference signals with similar frequencies. Furthermore, the next phase of work will also emphasize amplitude correction technology for the reconstructed signal. The harmonic spectrum method, derived from this approach, can serve as the preferred solution for identifying space waves in complex noise interference environments and will be applied to future monitoring of eLoran signals and space wave delay assessments.

Author Contributions: M.W. and X.J. conceived the content and structure of the paper; X.J. Analyzed simulation data and wrote papers; X.Q., J.D. and T.Y. helped with discussion and revision; X.J. and X.Q. completed data collection and the software code to analyze the data. All authors have read and agreed to the published version of the manuscript.

Funding: This work was supported by the National Natural Science Foundation of China, grant number 42174051.

Data Availability Statement: The data will be made available upon request

Acknowledgments: During the preparation of this study, the authors used MATLAB R2023b and Origin2022 for the purposes of Simulation Analysis and drawing. The authors have reviewed and edited the output and take full responsibility for the content of this publication.

Conflicts of Interest: The authors declare no conflicts of interest.

Abbreviations

The following abbreviations are used in this manuscript:

BDS	BeiDou navigation satellite
GPS	Global positioning system
GLONASS	Global navigation satellite system
GNSS	Global navigation satellite system
eLoran	Enhanced long-range navigation
PNT	Positioning, navigation, and timing
ECD	Envelope to cycle difference
IFFT	Inverse fast Fourier transform

APFFT	All-phase fast Fourier transform
MUSIC	Multiple signal classification
FIR	Finite impulse response
IIR	Infinite impulse response
WD	Wavelet decomposition
NTFT	Normal time-frequency transforms
VSS-LMS	Variable step size least mean square
LMS	Least mean square
SNR	Signal-to-noise ratio
RMS	Root mean square
RSME	Root mean square error
R	Correlation coefficient
R-RMSE	Relative root mean square error
NCC	Normalized correlation coefficient

572

References

1. Son, P.-W.; Park, S. G.; Han, Y.; Seo, K.; Fang, T. H. Demonstration of the Feasibility of the Korean eLoran System as a Resilient PNT in a Testbed. *Remote Sens.* **2023**, *15* (14), 3586. https://doi.org/10.3390/rs15143586.
2. Chang, S.; Ji, B.; Wu, M.; Bian, S.; Li, W.; Du, H. Evaluation of Height Correction on Loran Signal's Groundwave Transmission Delay Model. *IEEE Antennas Wirel. Propag. Lett.* **2023**, *22* (5), 1005–1009. https://doi.org/10.1109/LAWP.2022.3230554.
3. Wu, M.; Di, J.; Xu, J.; Li, F. Application and development of eLoran. *Hydrogr. Surv. Charting* **2022**, *42*, 44–49. https://d.wanfangdata.com.cn/Periodical/hych202204011.
4. Wu, M.; Zhu, Y.; Li, F.; Xu, J. *Radio Navigation Principle and Signal Receiving Technology*; National Defense Industry Press: Beijing, China, **2015**; ISBN 978-7-118-09795-5.
5. Pelgrum, W. New Potential of Low-Frequency Radionavigation in the 21st Century. Ph.D. Thesis, TU Delft, Delft, The Netherlands, **2006**.
6. Yin, K.; Wu, J.; Ning, R.; Chen, Y.; Liu, Q.; Wang, K. Preliminary Evaluation and Analysis of Differential Technology Performance of eLoran Timing System. *Electronics* **2025**, *14* (4), 789. https://doi.org/10.3390/electronics14040789.
7. Johnson, G. W.; Dykstra, K.; Oates, C.; Swaszek, P. F.; Hartnett, R. Navigating Harbors at High Accuracy Without GPS: eLoran Proof-of-Concept on the Thames River; **2007**; pp 1201–1211. http://www.ion.org/publications/abstract.cfm?jp=p&articleID=7215.
8. Zhu, Y.; Xu, J.; Wang, H.; Cao, K.; Hu, D. A New Sky-Groundwave Identification Algorithm for Loran-C Based on IFFT Spectral Division. *Electron. Inf. Technol.***2009,** *31*, 1153–1156. https://d.wanfangdata.com.cn/Periodical/dzkxxk200905031.
9. Li, J.; Xu, J.; Li, B.; He, H. Design and Implementation of Loran-C front Digital Band Pass Filter. *Appl. Electron. Tech.***2012**, *38*, 42–45+49. https://d.wanfangdata.com.cn/Periodical/dzjsyy201208013.
10. Lin, H.; Zhou, M.; Zhu, S.; Wang, K. A Frequency-Domain Suppression Method for Loran-C Narrowband Interference Based on apFFT. J. *Nav. Aeron. Eng.***2012**, *27*, 613–617. https://d.wanfangdata.com.cn/Periodical/SciencePaper201307170000203263.
11. Zeng, H.; Hua, Y.; Li, S. A Method Based on MUSIC Algorithm for Distinguishing between Sky-Wave and Ground-Wave. *J. Time Freq.***2011**, *34*, 53–59. https://d.wanfangdata.com.cn/Periodical/sxtwttk201101009.
12. Chen, J. Cross-Rate Interference Suppression Technology in Loran-C Based on Comb Filter. *Mod. Navig.***2022**, *13*, 41–45. https://d.wanfangdata.com.cn/Periodical/xddh202201009.
13. Zhu, Y.; Cao, K.; Cui, G.; Hu, D. An Improved Joint Denoising Method for Loran-C Signal. *Electron. Meas. Tech.***2008**, *31*, 21–23+43. https://d.wanfangdata.com.cn/Periodical/dzcljs200811006.
14. Yi, Q.; Deng, Z.; Zhao, J. Digital filter design of eLoran receiver. J. *Hebei Acad. Sci.* **2019**, *36*, 17–25. https://d.wanfangdata.com.cn/Periodical/hbskxyxb201901005.
15. Cheng, L.; Zhang, S.; Qi, Z.; Wang, X.; Chen, Y.; Feng, P. Research on eLoran Weak Signal Extraction Based on Wavelet Hard Thresholding Processing. *Remote Sens.* **2024**, *16* (16), 3012. https://doi.org/10.3390/rs16163012.
16. Liu, L.; Su, X.; Wang, G. Discussion on normal Time-Frequency Transform. *J. Navig*ation. *Position.***2016**, *4*, 1–4+23. https://d.wanfangdata.com.cn/Periodical/dhdwxb201604001.
17. Wang C.; Xu G.; Su, X.; Zhang Y.; Zhao Y.; Mu J. FBPBPF and NTFT are Used to Extract the Weak Periodic Component of Polar Motion and Analyze Its Excitation Reasons [J]. *Progress in Geophysics*, **2025**, *40*(3):905-912.https://d.wanfangdata.com.cn/Periodical/dqwlxjz202503003 (accessed 2025-11-22).
18. Liu, S.; Hua, Y.; Zhang, S. A Cycle Identification Algorithm for enhanced Long Range Navigation Signal Based on Skywave Reconstruction Technology. *Electron. Inf. Technol.***2022**, *44*, 3592–3601.https://d.wanfangdata.com.cn/Periodical/dzkxxk202210028.
19. Ponikvar, D.; Zupanic, E.; Jeglic, P. Magnetic Interference Compensation Using the Adaptive LMS Algorithm. *Electronics* **2023**, *12* (11), 2360. https://doi.org/10.3390/electronics12112360.
20. Wang, P.; Ma, K.; Wu, C. Segmented Variable-Step-Size LMS Algorithm Based on Normal Distribution Curve. J. *Natl. Univ. Def. Technol.* **2020**, *42*, 16–22. https://d.wanfangdata.com.cn/Periodical/gfkjdxxb202005003.
21. Wu, M.; Liu, L.; Li, F.; Zhu, B.; Li, W.; Jin, X. An Envelope-to-Cycle Difference Compensation Method for eLoran Signals in Seawater Based on a Variable Step Size Least Mean Square Algorithm. *Electronics* **2025**, *14* (3), 597. https://doi.org/10.3390/electronics14030597.
22. Tong, W. Research on front-end signal processing in Loran-C receiver. Master's thesis, Xidian University,**2007**. https://d.wanfangdata.com.cn/Thesis/Y1035851.

23. Gao, Y.; Xie, S. A Variable Step Size LMS Adaptive Filtering Algorithm and Its Analysis. *Acta Electron. Sin.* **2001**, *29*, 1094–1097. https://d.wanfangdata.com.cn/Periodical/dianzixb200108023.
24. Sun, W.; Wang, C. Power signal denoising based on improved soft threshold wavelet packet network. J. *Nav. Univ. Eng.* **2019**, *31*, 79–82. https://d.wanfangdata.com.cn/Periodical/hjgcdxxb201904014.
25. Liu, C.; Ma, L.; Pan, J.; et al. PD signal denoising based on VMD and improved wavelet threshold. *Mod. Electron. Tech.* **2021**, *44*, 45–50. https://d.wanfangdata.com.cn/Periodical/xddzjs202121010.
26. Zhang, P.; Li, X.; Cui, S. An improved wavelet threshold-CEEMDAN algorithm for ECG signal denoising. *Comput. Eng. Sci.* **2020**, *42*, 2067–2072. https://d.wanfangdata.com.cn/Periodical/wthtjsjs202106002.
27. Liu, F.; Lü, Z.; Zhang, C.; Ma, Z. Research on Speech Enhancement Algorithm Based on Modified Wavelet Threshold Function. *Signal Process.* **2016**, *32*, 203–213. https://d.wanfangdata.com.cn/Periodical/xhcl201602011.
28. Qiao, Y.; Li, Q.; Qian, H.; Song, X. Seismic signal denoising method based on VMD and improved wavelet threshold. Comput. Tech. *Geophys. Geochem. Explor.* **2021**, *43*, 690–696. https://d.wanfangdata.com.cn/Periodical/wthtjsjs202106002.
29. GB/T 12752-1991; General Specification for Marine Loran-C Receiving Equipment. The State Bureau of Quality and Technical Spervision: Beijing, China, 1991. Available online: https://www.renrendoc.com/p-881056.html (accessed on 26 May 2025)
30. Cai, S.; Ye, R.; Wang, Q.; Liu, L. Tide analysis and prediction based on inaction principle. *Hydrogr. Surv. Charting* **2021**, *41*, 47–51. https://d.wanfangdata.com.cn/Periodical/hych202103011.
31. Yao, Y.; Liu, L.; Sheng, M.; Xu, H. Unbiased picking onset time of P and S phases by Normal Time-Frequency Transform method under a strong noise environment. Chin. J. *Geophys.* **2022**, *65*, 227–243. https://d.wanfangdata.com.cn/Periodical/dqwlxb202201018.

Disclaimer/Publisher's Note: The statements, opinions and data contained in all publications are solely those of the individual author(s) and contributor(s) and not of MDPI and/or the editor(s). MDPI and/or the editor(s) disclaim responsibility for any injury to people or property resulting from any ideas, methods, instructions or products referred to in the content.